Removal of Nonylphenol Polyethylene Glycol (NPEG) with Au-TiO$_2$ Catalysts: Kinetic and Initial Transformation Path

Claudia Aguilar [1,*] , **Mayra Garcia** [1] , **Carlos Montalvo** [1] , **Francisco Anguebes** [1] , **Edgar Moctezuma** [2] , **Mohamed Abatal** [3] **and Sandra Figueroa** [3]

[1] Facultad de Química, Universidad Autónoma del Carmen, Calle 56 No. 4 Av. Concordia, Ciudad del Carmen 24180, Campeche, Mexico; maje180894@gmail.com (M.G.); cmontalvo@pampano.unacar.mx (C.M.); fanguebes@pampano.unacar.mx (F.A.)

[2] Facultad de Ciencias Químicas, Universidad Autónoma de San Luis Potosí, Av. Dr. Manuel Nava No.6, Zona Universitaria, San Luis Potosí 78210, S.L.P., Mexico; edgar@uaslp.mx

[3] Facultad de Ingeniería, Universidad Autónoma del Carmen, Avenida Central S/N, Mundo Maya, Ciudad del Carmen 24115, Campeche, Mexico; mabatal@pampano.unacar.mx (M.A.); sfigueroa@pampano.unacar.mx (S.F.)

* Correspondence: caguilar@pampano.unacar.mx

Abstract: The purpose of this study was to evaluate the efficiency of the Au-TiO$_2$ catalyst in the degradation of nonylphenol polyethylene glycol (NPEG). In the first part of the study, the catalyst was synthesized and characterized. Initially, the catalyst (TiO$_2$ Degussa P-25) was doped with gold precursor salts (HAuCl$_4$) at different concentrations (5, 10, and 15%) and the photodeposition method with UV light. It was determined by diffuse reflectance (DF) and scanning electron microscopy (SEM) that the photodeposition method was effective for the inclusion of gold particles on the surface. The catalyst band gap showed a reduction to 2.9 e.v (compared to TiO$_2$ Degussa P-25), and it was observed that the gold-doped catalyst showed absorption in the visible light range 500 to 600 nm. The percentage of deposited gold was determined by energy dispersive spectroscopy (EDS). In the second part of the study, various NPEG degradation experiments were performed; with the catalyst that showed the best conversion percentages of NPEG, the experimental data were analyzed using UV-Vis spectrophotometry and TOC (total organic carbon). With these results, a carbon-based mass balance and reaction kinetics were generated using the Langmuir–Hinshelwood (L–H) heterogeneous catalysis model. For the estimation of the kinetic constants, the non-linear regression of the Levenger–Marquardt algorithm was used. With these results, kinetic models of the degradation of the molecule and the generation and consumption of organic intermediate products (OIPs) were generated.

Keywords: photocatalytic degradation; ethoxylated alkylphenols; gold titanium catalyst

1. Introduction

Today, many compounds are classified as emerging pollutants, including drugs, personal hygiene products, among others [1]. A special class of these pollutants is called alkylphenol ethoxylates (APEs); it is used the plastics industry and as a surfactant in numerous commercial products. Recent studies have shown the presence of alkylphenols and their derivatives in sediments and waters; although the authors consider that the risk factors for organisms are still low, the potential danger from the increase in these compounds may be of utmost importance in the coming years [2]. Likewise, Huang et al. [3] also reports concentrations of these components in different substrates, and their studies find a direct

relationship to months with low rainfall [4]. Biodegradation of APEs during wastewater treatment and subsequent discharge into the environment can result in small ethoxy chains giving way to hydrophobic metabolites, the biodegradation of which results in the production of nonylphenol-mono- and di-ethoxylate, nonylphenoxy ethoxyacetic acid, and nonylphenol, which is more recalcitrant and more toxic than other nonylphenol (NPEO) precursors [5].

The reviews by Priac et al. [6] describe different processes for the elimination of emerging contaminants. These processes can involve membranes, physical removal, biotechnological processes, the use of powerful adsorbents (whether conventional or unconventional), and advanced oxidation processes (photocatalysis, photolysis, and sonochemistry).

The toxicity of APEs is not high, although its degradation is slow and produces secondary compounds that may have ethoxylated groups in their structure and that behave as endocrine disruptors [5]. APEs inhibit microorganisms that reduce organic matter in treatment plants and they produce foams that limit oxygen transport processes.

Conventional treatments are inadequate or deficient for the elimination of emerging contaminants; advanced oxidation processes are a viable alternative [7]. Photocatalysis has proven to be efficient in eliminating these pollutants [8,9].

Certain processes such as "charge recombination" decrease the efficiency of a photocatalytic process [10]. In this sense, the doping of the catalyst with metallic elements can reduce this process (by the sequestration of electrons), and the photogenerated holes can remain available for reaction [11]. The effect of gold on different semiconductors shows an increase in the transformation of the specific surface, which improves the photocatalytic activity and improves the separation of the electron-hole pair [12,13].

Particular gold nanoparticles in titanium have been used as photocatalysts in the degradation of dyes [14,15], phenol, and phenolic compounds [2,12,13,16]. In this sense, Dozzi et al. [17] show that the presence of gold in TiO_2 facilitates the mineralization of formic acid, whose degradation comes mainly from the direct interaction with the holes of the photoproduced valence band. In this same study, it is concluded that intermediate species can contribute to keep gold in metallic form.

Gold on titanium dioxide is a catalyst which shows excellent results in photocatalytic reactions. These processes are a viable alternative for the removal of nonylphenol polyethylene glycol (NPEG), and the study of their reaction kinetics represents an advance in the understanding of the removal phenomena of this component.

2. Results and Discussion

2.1. SEM and EDS

The superficial morphological analysis for secondary electrons and chemical analysis by EDS were carried out in a Sweeping Dual Beam ((focused ion beam) FIB/SEM) Electron Microscope FEI-Helios Nanolab 600 to determine the elemental composition of the $Au-TiO_2$ catalyst (Figure 1 and Table 1).

Table 1. Elemental composition of the catalysts doped with gold particles by weight percentage deposited on TiO_2 P-25 catalyst and determined by EDS.

Catalyst	Elements in Wt (%)		
	O_2	Ti	Au
$Au-TiO_2$ (5%)	43.52	53.86	2.62
$Au-TiO_2$ (10%)	44.77	49.83	5.40
$Au-TiO_2$ (15%)	43.85	43.40	12.75

Small Au particles can induce greater changes in the Fermi level compared to particles with larger diameters [16,18]. The photodeposition method is usually effective in generating smaller particles than

those generated by other methods; this behavior may be due to the fact that titanium behaves as an electron deposit when subjected to UV radiation and modifies its Fermi energy level [19].

Figure 1 shows the micrographs of the synthesized photocatalysts, which mainly revealed spherical crystals of TiO_2. In addition, sphere-shaped Au particles were observed, which were distributed over the TiO_2.
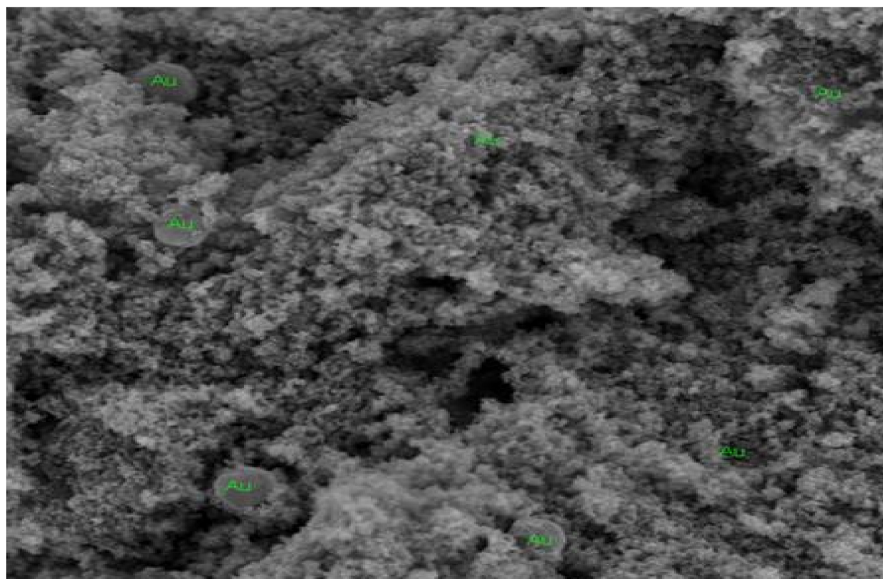

Figure 1. Scanning electron microscopy images of titanium catalysts doped with gold particles. Microscopy image showing the surface of the catalyst with a concentration of 5% (theoretical) of deposited gold.

2.2. Surface Area

Figure 2 shows the typical nitrogen adsorption-desorption isotherms of the samples analyzed, which are based on the BET (Brunauer–Emmett–Teller) isotherm. In addition to determining the surface area, the total pore volume and average pore diameter were also determined: superficial area (m^2/g) = 47.57; Vm (cm^3/g) = 10.931; total pore volume (cm^3/g) = 0.3648; average pore diameter (nm) = 30.668. BET analysis was performed for only the catalyst that showed the best NPEG-removal percentages (Au-TiO_2 at 5%).
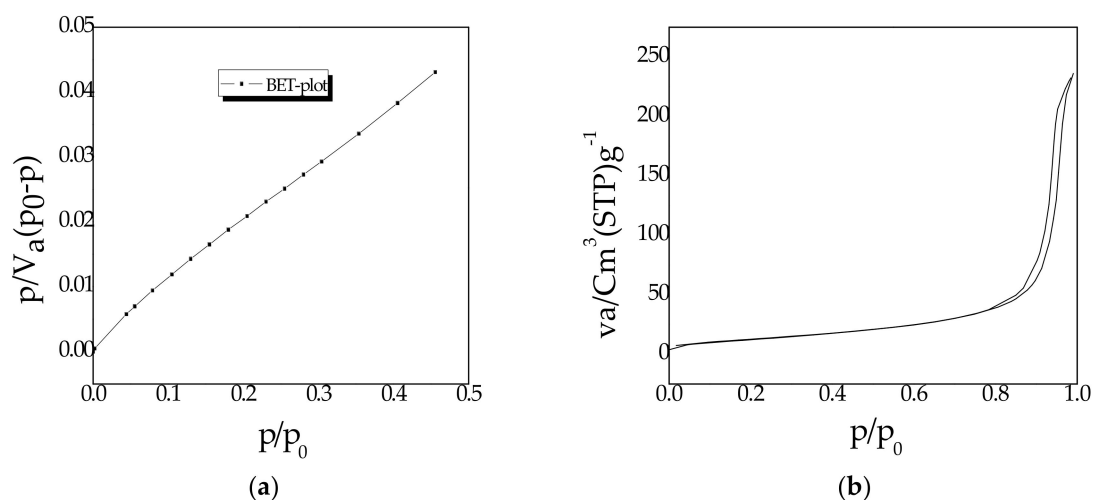

Figure 2. Adsorption/desorption isotherms of the catalyst by nitrogen physisorption: (**a**) curve of the BET isotherm; (**b**) desorption/adsorption curve for surface area determination.

2.3. Diffuse Reflectance

For the determination of the band gap, the doped catalysts were analyzed by UV spectroscopy using a Shimadzu UV-2450 (Autonomous University of San Luis Potosí; UASLP, San Luis Potosí, México) with an ISR-2200 Integrating Sphere Attachment. Measurements were taken in the range of wavelength between 200 and 600 nm.

Figure 3a shows the comparison between the three doped catalysts and the commercial catalyst (TiO_2 Degussa P-25); the absorption differences in the range of 500–600 nm are attributed to the presence of gold particles deposited on the solid.
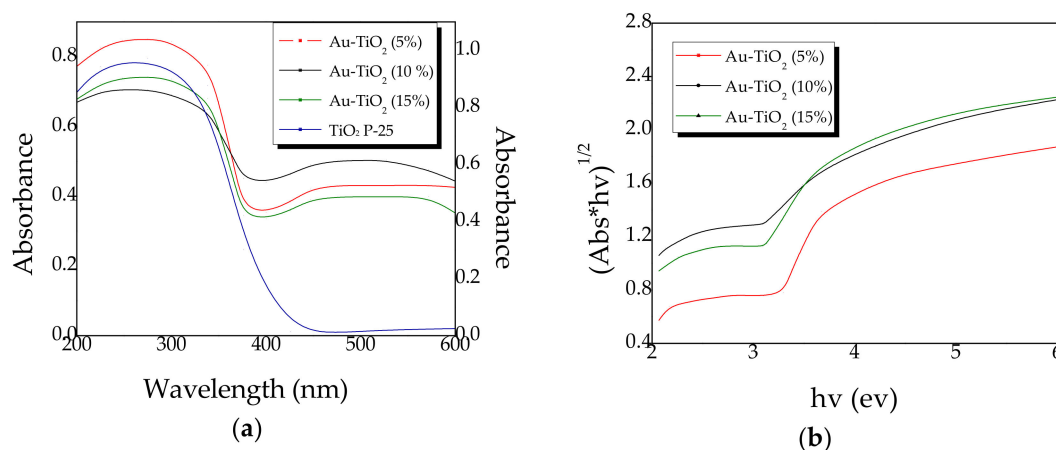

Figure 3. (**a**) Kubelka Munk plots of the Au-TiO_2 catalysts and the TiO_2 P-25 catalyst. (**b**) Normalization of diffuse reflectance data for band gap calculation.

A semiconductor experiences a charge balance when it is in an excited state and in contact with metallic gold nanoparticles. This balance has a direct influence on the Fermi energy levels by changing to more negative potentials [20], which improves the photocatalysis processes; however, according to these investigations, there is a dependence on the size of the gold particle deposited in the semiconductor. Likewise, the presence of metallic elements can increase the properties and electrical conductivity of a semiconductor when it is doped [21].

Through equations $E_g = \frac{h_c}{\lambda_g} = \frac{h(v\lambda_g)}{\lambda_g} = hv$, $v = \frac{c}{\lambda_g}$ and $(Abs * hv)^{1/2}$ in function of hv (Figure 3b), the value of the E_g is determined (Table 2), where λ_g = wavelength (nm), h = Planck constant, and c = speed of light in a vacuum.

Table 2. Values of the band gap (Eg).

Catalyst	Eg (ev)
Au-TiO_2 at 5%	2.9
Au-TiO_2 at 10%	2.9
Au-TiO_2 at 15%	2.9
TiO_2 P-25	3.1

According to the results obtained, the theoretical amount of gold particles that were deposited on the surface of the semiconductor had no influence on modifying the band gap compared to the undoped catalyst.

2.4. Kinetics of Photocatalytic Degradation

Initially, to test the efficiency of the doped catalysts, an NPEG degradation test was carried out at a concentration of 50 mg/L. The conversion percentages achieved showed that the Au-TiO_2 at 5% catalyst had the best results; based on these tests, it was determined that the entire kinetic study would

be performed with this catalyst. The concentration of the contaminant is a very important variable in photocatalytic processes. The initial concentration of the NPEG varied between 20 and 160 mg/L, with a fixed mass of the catalyst at 2 g/L (0.2 g of TiO_2/100 mL of solution). The volume of the solution was 250 mL and the flow of oxygen was 100 cm^3/min. In all cases, samples of the reaction mixture were taken for analysis with UV and total organic carbon (TOC). The results of these experiments are shown in Figure 4a, which shows the NPEG concentration as a function of reaction time.
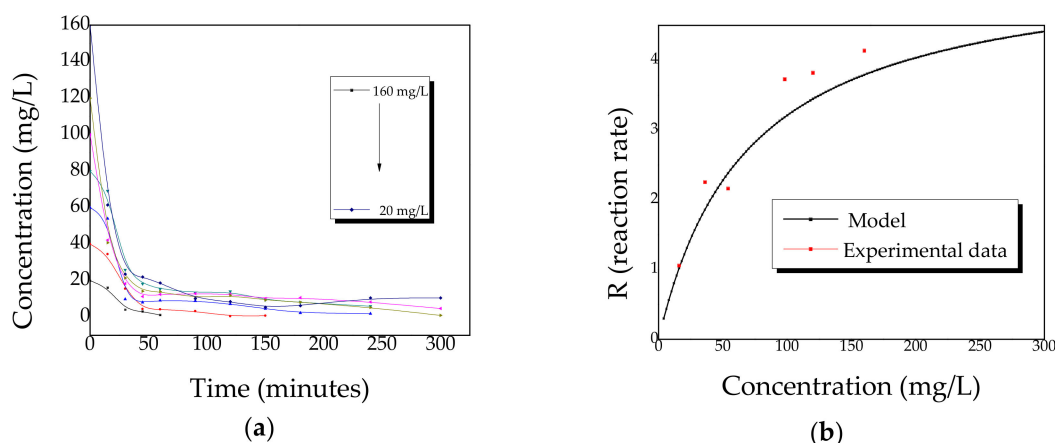

Figure 4. (**a**) nonylphenol polyethylene glycol (NPEG) concentration (mg/L) as a function of time, degradation profile at different reaction times, (catalyst concentration = 2 g/L, total volume = 250 mL, amount of oxygen = 100 cm^3/min). (**b**) Estimation of the Langmuir–Hinshelwood (L–H) model applied in the degradation of NPEG.

According to the principles of photocatalysis [21], the oxidation of organics proceeds through hydroxylation between the HO· radicals generated and the organic component. The behavior of a photocatalytic reaction can be explained in terms of the L–H equation for heterogeneous catalysis [11,22].

$$-r_{NPEG} = -\frac{dC_{NPEG}}{dt} = \frac{K_1 C_{NPEG}}{1 + K_2 C_{NPEG} + \sum K_i C_{OIP}} \tag{1}$$

where $-r_{NPEG}$ is the decomposition rate of the NPEG, C_{NPEG} is the concentration of NPEG, and $\sum K_i C_{OIP}$ is the concentration of all organic intermediate products (OIPs).

If one analyzes the experimental data in short reaction times, it is possible to overlook the absorption term for the intermediate products. The kinetics constant (K_1) and the adsorption constant (K_2) were calculated by nonlinear regression; the values for the constants K_1 and K_2 are 0.07848062 (min^{-1}) and 0.1444828 $(mg/L)^{-1}$, respectively. In order to validate the L–H model, the experimental reaction rates and the reaction rates calculated with Equation (2) were plotted on Figure 4b.

$$-r_{NPEG} = -\frac{dC_{NPEG}}{dt} = \frac{K_1 C_{NPEG}}{1 + K_2 C_{NPEG}} \tag{2}$$

The estimation of the rate constant K_1 indicated that the reaction followed pseudo-first-order kinetics. The main changes in concentration were shown in the first minutes of reaction for this reason. It is considered that the L–H model is usually not sufficient to evaluate its kinetics; a series reaction was proposed whose global equation (Equation (3)) expresses two stages and two kinetic constants, assuming first-order behavior. NPEG breaks down through intermediate products, which finally decompose into CO_2

$$NPEG \overset{K_A}{\to} OIP \overset{K_B}{\to} CO_2 \tag{3}$$

For the evaluation of NPEG decomposition, a kinetic of the first order was taken to be expressed in Equations (4) and (5).

$$-\frac{dC_{NPEG}}{dt} = K_A C_{NPEG} \tag{4}$$

$$C_{NPEG} = C_{NPEG\,0}\, e^{-K_A t} \tag{5}$$

The formation of OIPs can be represented by the following equations (Equations (6) and (7)).

$$\frac{dC_{OIP}}{dt} + K_B C_{OIP} = K_A C_{NPEG\,0}\, e^{-K_A t} \tag{6}$$

$$C_{OIP} = \frac{K_A C_{NPEG\,0}}{K_B - K_A}\, e^{-K_A t} \tag{7}$$

The formation of the final product CO_2 was also evaluated, using Equations (8) and (9).

$$\frac{dC_{CO_2}}{dt} = K_B C_{OIP} \tag{8}$$

$$C_{CO_2} = -\frac{K_B C_{NPEG\,0}}{K_B - K_A}\, e^{-K_A t} \tag{9}$$

The value of the kinetic constants was calculated on the basis of non-linear regression using the Levenger–Marquardt algorithm (statistical package "Statistical 7.1"). The values of the kinetic constants were $K_A = 0.052242$ (min^{-1}) and $K_B = 0.02317$ (min^{-1}).

The OIP concentration was calculated on the basis of a mass balance (a typical curve for these parameters is shown with a concentration of 20 mg/L), using the results of the NPEG concentration and the TOC values (Figure 5). The data were obtained by UV spectroscopy and mineralization behavior followed by TOC. These two parameters were useful for estimating and obtaining the average OIP curve using the following equation:

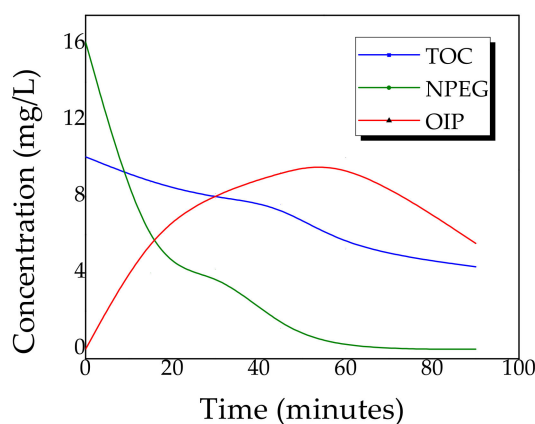$$TOC - C_{CARBON}NPEG = C_{CARBON}OIP \tag{10}$$

Figure 5. Reaction behavior: total organic carbon (TOC) represents the total organic carbon of the mineralization of the NPEG; NPEG = 20 mg/L, measured by UV spectroscopy; organic intermediate products (OIPs) = obtained by mass balance.

The results of the application of Equation (5) for NPEG degradation are shown in Figure 6, and the results for predicting the formation and consumption of the OIPs (Equation (7)) are shown in Figure 7.
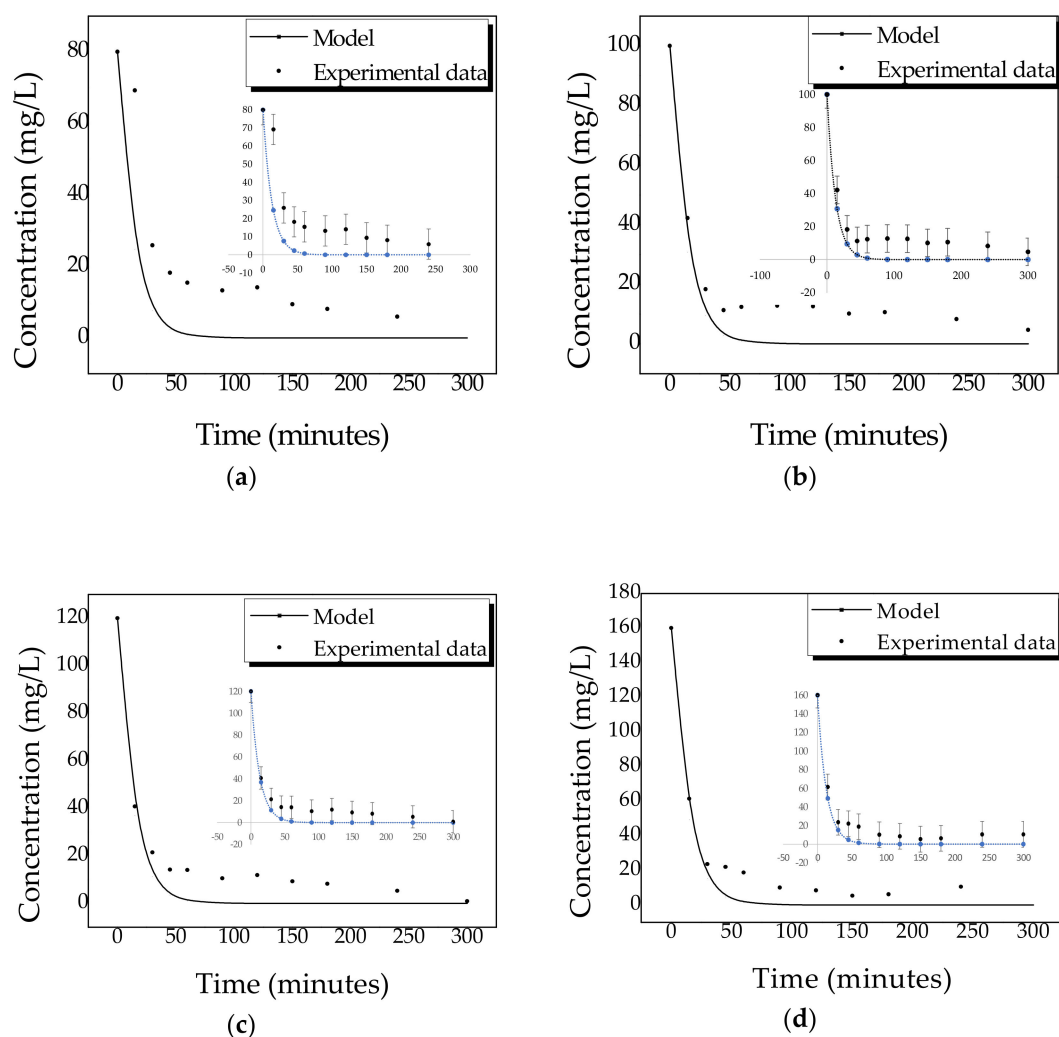
Figure 6. NPEG degradation profile at different concentrations: (**a**) 80 mg/L, (**b**) 100 mg/L, (**c**) 120 mg/L, and (**d**) 160 mg/L. The curve generated with the application of the first-order model and the experimental data obtained by UV-Vis spectroscopy is shown. In each case, the absolute error value was estimated from the experimental data with respect to the model. For curve (**a**), the error ranges from 5.899–18.304; for the curve (**b**), the error ranges from 4.699–12.591; for curve (**c**), the error ranges from 0.899–12.918; and for curve (**d**), the error ranges from 5.358–17.318.

However, the equation for predicting CO_2 formation could not be modeled under first-order kinetics with a serial reaction; this was because there were losses to the atmosphere that cannot be quantified with the analytical tools available. However, the first-order model adequately predicted the degradation of NPEG, as well as the formation and consumption of OIPs. With the results obtained, it was concluded that the degradation of NPEG as the formation and consumption of the OIPs followed first-order kinetics, which could be seen in the concentration decrease profile that was observed in all the reactions and which had a considerable decrease during the first 50 min before the reaction became pseudo-stationary.

In order to establish the OIPs that are formed and consumed during the reaction, FTIR tests were carried out. Reaction samples were treated with ethyl acetate and Micro Extraction in Solid Phase (SPEM) with Licrohout cartridges, and then analyzed using FTIR.

Figure 8a shows the spectra at the start time and after four hours of reaction, where the permanence of the disubstituted aromatic group can be observed (669 and 942 cm^{-1}, respectively), as well as its isomerization (868 cm^{-1}). Likewise, the functional groups belonging to C-O-R (1014 cm^{-1}) and R-OH (1115 cm^{-1}) persist, indicating a fragmentation of the ethoxylate chain. The formation of

carboxylic acids at a wavelength ranging from 1136–1250 cm^{-1}, 2540–2690 cm^{-1}, and 3000–3400 cm^{-1} is highlighted, the latter also being representative for the possible exit of the ethoxylate functional group giving way to the generation of R-OH groups.
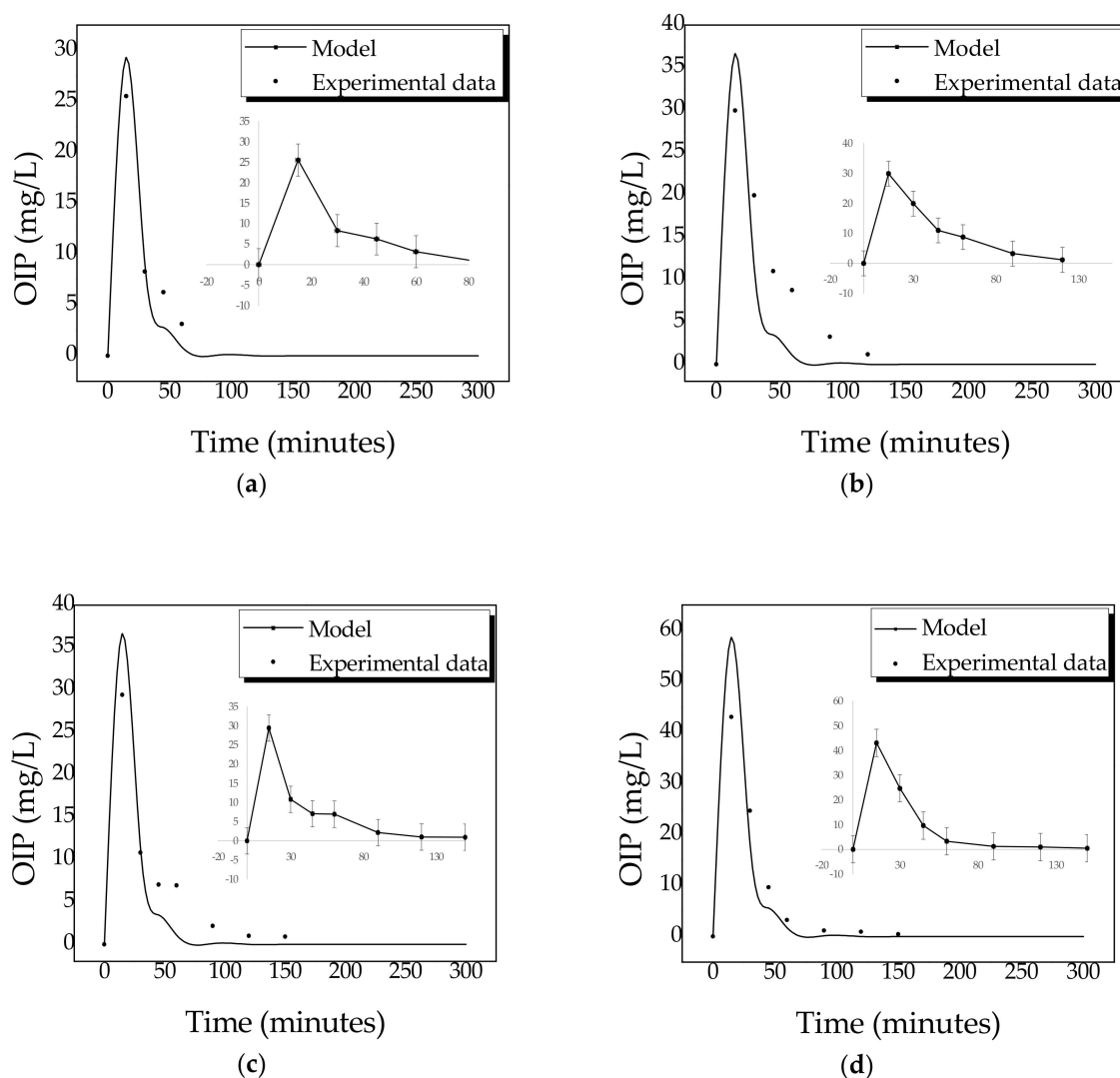

Figure 7. Profile of the generation and consumption of OIPs showing the curve generated by the model and experimental data obtained by a carbon-based mass balance at different initial concentrations: (**a**) 80 mg/L, (**b**) 100 mg/L, (**c**) 120 mg/L, and (**d**) 160 mg/L. In each case, the error graph is attached and related to the model and the experimental data. For (**a**) the absolute error is in the range of 2.282–3.793; for (**b**), the absolute error is in the range of 1.1603–8.6391; for (**c**), the absolute error is in the range of 0.9903–7.2276; and for (**d**), the absolute error is in the range 0.4385–12.321.

Table 3 lists, for comparison, the information obtained in the spectra before and after photodegradation at 300 mg/L.

The reaction is fast and, as shown in Figure 8b, after two hours of reaction the signal corresponding to a type of π-π transition (280 nm) of the aromatic ring decreased, and did so considerably between four and six hours of reaction. Likewise, the signals that correspond to single bonds (225 nm) decreased; according to Salomon et al. [23], this type of molecules is initially degraded with the loss of the ethoxylate group. Chen et al. [24], in their research with photolysis, showed that the degradation pathway proceeds through the shortening of ethylene oxide side chains and the oxidation of the alkyl chain, with the generation of intermediates having an alkyl chain and carboxylated ethoxylate.

In this work, with the analytical techniques used, it was concluded that there was chemical degradation of the molecule, beginning with the fragmentation of the ethoxylated chain, as well as the degradation of the aromatic ring.
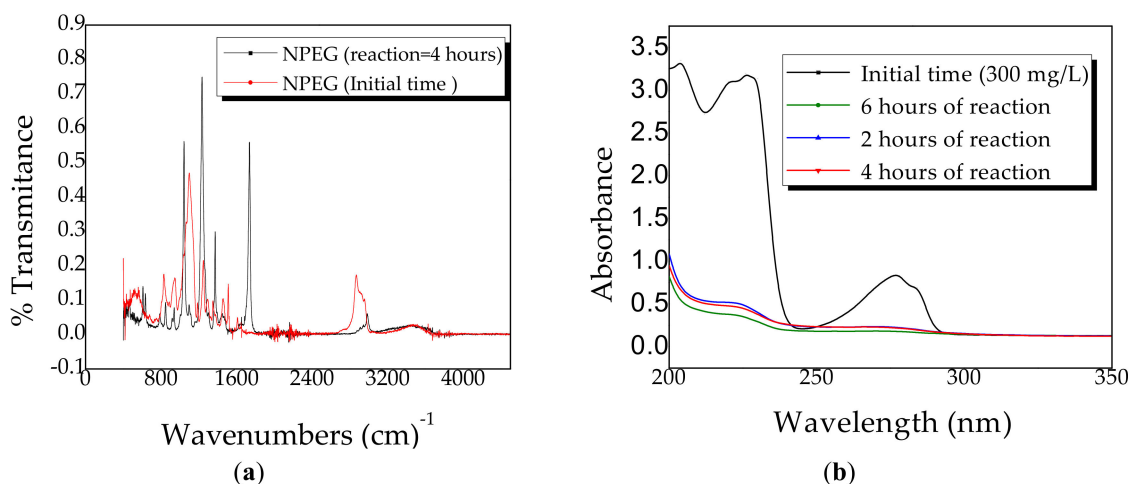

Figure 8. (**a**) NPEG FTIR spectrum at different reaction times; (**b**) NPEG-UV spectrum at different reaction times.

Table 3. Summary of the structures detected by FTIR in a NPEG reaction sample.

Wavenumber (cm^{-1})	Functional Group
835	Aromatic for disubstituted
11,021,189	R-OH
1250	C-O-R
1350	R-OH
1450–2000	Aromatic ring
2875–2961	C-H
3200–3650	R-OH

3. Materials and Methods

To deposit metallic gold on the catalyst surface, the photodeposition method was used. The theoretical amount of precursor salt to be used in each case was determined with the following equation.

$$W_{HAuCl_4} = \frac{(W_{Au})\left(MW_{HAuCl_4}\right)}{(MW_{Au})}$$
(11)

where W_{HAuCl_4} = weight of HAuCl$_4$, MW_{HAuCl_4} = molecular weight of HAuCl$_4$, W_{Au}= weight of gold, and MW_{Au} = molecular weight of gold.

In each case 0.5 g of TiO$_2$ were placed in a glass reactor with the appropriate amount of salts and 100 mL of deionized water. The reaction system was continuously stirred (in the dark phase) for a period of time. Subsequently, the solution was irradiated for 5 hours (4 UV lamps of 365 nm), with the addition of nitrogen (80 cm^3/min) (INFRA Corporation, Carmen City, Mexico). The water was removed by vacuum filtration, which was followed by drying at 100 °C and calcination at 550 °C; this temperature has been shown to be optimal in a semiconductor doping process [25]. Other studies have shown that for the oxidation of dyes, photocatalysts calcined between 550 and 625 °C show greater activity [26]. Furthermore, the crystalline form of the semiconductor depends on the calcination temperature [27]. After obtaining the catalysts, tests were carried out to determine the efficiency and the selection of one of them to continue with the kinetic study.

Three catalysts were doped with different theoretical concentrations of gold particles. The commercial catalyst Degusa P-25 was used (Evonik Degussa México S.A de C.V., CDMX, México).

4-Nonylphenyl-polyethylene (CAS number: 9016-45-9) was used as a model pollutant. $HAuCl_4$ (Sigma Aldrich, Química S.de R.L de C.V, México) was used as a precursor for gold ions. Reaction samples were filtered for catalyst separation using 0.22 mm cellulose filters (MilliporeCorp, Billerica, MA, US). The surface morphological analysis by secondary electrons and chemical analysis by energy dispersive spectroscopy were performed in an FEI-Helios Nanolab 600 Dual Beam Scanning Electron Microscope (FIB/SEM), from the National Laboratory of Research in Nanoscience and Nanotechnology (LINAN, San Luis Potosí, México). Diffuse reflectance analyses were performed in the spectrum Shimadzu UV-2450, equipped with the ISR-2200 Integrating Sphere Attachment accessory (Autonomous University of San Luis Potosí; UASLP, San Luis Potosí, México).

The surface area was determined with Belsorp II equipment, at the Civil Engineering Institute of the Autonomous University of Nuevo León (UANL), San Nicolás de los Garza, México. Solid-phase microextraction equipment with Licrohout cartridges was used to extract the organic phase from NPEG reaction samples. Infrared spectroscopy (FTIR) analyses were performed using a spectrophotometer from the Agilent Technologies-Cary 600 brand in conjunction with a GladiATR from the Pike Technologies brand (UNACAR, City of Carmen, México).

4. Conclusions

The photodeposition method is suitable for embedding gold particles on the surface of the semiconductor. In this study, the characteristics of the doped material indicate that the actual percentage of deposited metals is close to the theoretical amount; likewise, the reduction of its band gap makes it suitable for reactions in the presence of visible light. However, the mass of the dopant has no effect on the decrease in bandwidth since this value is the same even when the amount of mass of the gold particle precursor solutions is varied. If the surface area presents a reduction in comparison with Degussa P-25, the degradation of the NPEG produces an accelerated behavior in the first minutes of the reaction whereby it is considered to evaluate itself through the kinetics of a simple first-order reaction. The degradation pathway may begin with the fragmentation of the ethoxylated chain and the subsequent degradation of the aromatic ring.

Author Contributions: In this paper, C.A. and C.M. designed the experiments; M.G. performed the experiments; and E.M. allowed access to specialized equipment to perform the experiments. The manuscript was written by C.A. and C.M.; M.A., S.F., and F.A. collaborated in the review of the project. All authors have read and agreed to the published version of the manuscript.

Conflicts of Interest: The authors declare no conflict of interest.

References

1. Ebele, A.J.; Mohamed, A.; Elwafa, A.; Stuart, H. Pharmaceuticals, and personal care products (PPCPs) in the freshwater aquatic Environment. *Emerg. Contam.* **2017**, *3*, 1–16. [CrossRef]
2. Diao, P.; Chen, Q.; Wang, R.; Sun, D.; Cai, Z.; Wu, H.; Duan, S. Phenolic endocrine-disrupting compounds in the Pearl River Estuary: Occurrence, bioaccumulation and Risk assessment. *Sci. Total Environ.* **2019**, *584*, 1100–1107. [CrossRef] [PubMed]
3. Huang, B.; Li, X.; Sun, W.; Ren, D.; Li, X.; Liu, Y.; Li, Q.; Pan, X. Occurrence, removal, and fate of progestogens, androgens, estrogens, and phenols in six sewage treatment plants around Dianchi Lake in China. *Environ. Sci. Pollut. Res. Int.* **2014**, *21*, 12898–12908. [CrossRef] [PubMed]
4. Cheng, J.R.; Wang, K.; Yu, J.; Yu, Z.; Zhang, Z. Distribution, and fate modeling of 4-nonylphenol, 4-t-octylphenol, and bisphenol A in the Yong River of China. *Chemosphere* **2018**, *195*, 594–605. [CrossRef] [PubMed]

5.   Ying, G.G.; Willians, B.; Kookana, R. Environmental fate of alkylphenols and alkylphenolethoxylates—A review. *Environ. Int.* **2002**, *28*, 215–226. [CrossRef]

6.   Priac, A.; Morin-Crini, N.; Druart, C.; Gavoille, S.; Bradu, C.; Lagarrigue, C.; Giangiacomo, G.; Winterton, P.; Crini, G. Alkylphenol and alkylphenol polyethoxylates in water and wastewater: A review of options for their elimination. *Arab. J. Chem.* **2017**, *10*, S3749–S3773. [CrossRef]

7.   Chung, J.; Lam, S.M.; Mohamed, A.R.; Lee, K.T. Degrading Endocrine Disrupting Chemicals from Wastewater by TiO_2 Photocatalysis: A Review. *Int. J. Photoenergy* **2012**, *2012*, 185159.

8.   Philippe, K.K.; Timmers, R.; Grieken, R.V.; Marugan, J. Photocatalytic Disinfection and Removal of Emerging Pollutants from Effluents of Biological Wastewater Treatments, Using a Newly Developed Large-Scale Solar Simulator. *Ind. Eng. Chem. Res.* **2016**, *55*, 2952–2958. [CrossRef]

9.   Montalvo, C.; Aguilar, C.A.; Alcocer, R.; Ramírez, M.A.; Córdova, V.A. Semi-Pilot Photocatalytic Rotating Reactor (RFR) with Supported TiO_2/Ag Catalysts for Water Treatment. *Molecules* **2018**, *23*, 1–11.

10.   Syrek, K.; Grudzien, J.; Sennik, A.; Brudzisz, A.; Sulka, D. Anodic titanium oxide layers modified with gold, silver, and Cooper Nanoparticles. *J. Nanomater.* **2019**, *2019*, 9208734. [CrossRef]

11.   Aguilar, C.A.; Montalvo, C.; Zermeño, B.B.; Cerón, R.M.; Cerón, J.G.; Anguebes, F.; Ramirez, M.A. Photocatalytic degradation of acetaminophen, tergitol and nonylphenol with catalysts TiO_2/Ag under UV and Vis light. *Int. J. Environ. Sci. Technol.* **2018**, *16*, 843–852. [CrossRef]

12.   Romero, E.; Gutierrez, M.; Mugica, V.; González, L.; Torres, M.; Tzompantzi, F.J.; Tzompantzi, C. Synthesis and characterization of gold nanoparticles on titanium dioxide for the catalytic degradation of 2, 4 dichlorophenoxyaxetic acid. *J. Appl. Res. Technol.* **2018**, *16*, 346–356.

13.   Ayati, A.; Ahmadpour, A.; Bamoharram, F.; Tanhaei, B.; Manttari, M.; Sillanpaa, M. Review on catalytic applications of Au/TiO_2 nanoparticles in the removal of water pollutant. *Chemosphere* **2014**, *107*, 163–174. [CrossRef]

14.   Mondal, S.; Reyes, M.E.; Pal, U. Plasmon induced enhanced photocatalytic activity of gold loaded hydroxyapatite nanoparticles for methylene blue degradation under visible light. *RSC Adv.* **2017**, *7*, 8633–8645. [CrossRef]

15.   Sobhana, L.; Sarakha, M.; Prevot, V.; Fardim, O. Layered doublé hidroxides decotared with Au-Pd nanoparticles to photodegradate Orange II from water. *Appl. Clay Sci.* **2016**, *134*, 120–127. [CrossRef]

16.   Oros, S.; Pedraza, J.A.; Guzmán, C.; Quintana, M.; Moctezuma, E.; Del angel, G.; Gómez, R.; Pérez, E. Effect of Gold Particle Size and Deposition Method on the Photodegradation of 4-Chlorophenol by Au/TiO_2. *Top. Catal.* **2011**, *54*, 519–526. [CrossRef]

17.   Dozzi, M.V.; Prati, L.; Canton, P.; Selli, E. Effects of gold nanoparticles deposition on the photocatalytic activity of titanium dioxide under visible light. *Phys. Chem. Chem. Phys.* **2009**, *11*, 71–80. [CrossRef]

18.   Kamat, P. Photophysical, Photochemical and Photocatalytic Aspects of Metal Nanoparticles. *J. Phys. Chem. B.* **2002**, *106*, 7729–7744. [CrossRef]

19.   Jacob, M.; Levanon, H.; Kamat, P.V. Charge distribution between UV-irradiated TiO_2 and gold nanoparticles: Determination of shift in the Fermi level. *Nanoletters* **2003**, *3*, 353–358. [CrossRef]

20.   Subramanian, V.; Wolf, E.E.; Kamat, P.V. Catalysis with TiO_2/gold nanocomposites. Effect of metal particle size on the Fermi level equilibration. *J. Am. Chem. Soc.* **2004**, *126*, 4943–4950. [CrossRef]

21.   Loddo, V.; Bellardita, M.; Camera-Roda, G.; Parrino, F.; Palmisano, L. Heterogeneous Photocatalysis: A Promising Advanced Oxidation Process. In *Current Trends and Future Developments on (Bio-) Membranes*; Elsevier: Palermo, Italy, 2018. [CrossRef]

22.   Aguilar, C.; Abatal, M.; Montalvo, C.; Anguebes, F.; Ramírez, M.A.; Cantú, D. Removal of an Ethoxylated Alkylphenol by Adsorption on Zeolites and Photocatalysis with TiO_2/Ag. *Processes* **2019**, *7*, 1–15.

23.   Salomon, K.Y.; Huberson, N.G.; Sylvain, A.K. Nonylphenol and Its Ethoxylates in Water Environment. *J. Geogr. Environ. Earth Sci.* **2019**, *23*, 1–14. [CrossRef]

24.   Chen, L.; Zhou, H.Y.; Deng, Q.Y. Photolysis of nonylphenol ethoxylates: The determination of the degradation kinetics and the intermediate products. *Chemosphere* **2007**, *68*, 354–359. [CrossRef] [PubMed]

25.   Behpour, M.; Ghoreishi, S.M.; Razavi, S. Photocatalytic activity of TiO_2/Ag nanoparticle on degradation of water pollutions. *Dig. J. Nanomater. Biostruct.* **2010**, *5*, 467–475.

26. Haugen, A.B.; Kumakiri, I.; Simon, C. TiO$_2$, TiO$_2$/Ag and TiO$_2$/Au photocatalysts prepared by spray pyrolysis. *J. Eur. Ceram. Soc.* **2011**, *31*, 291–298. [CrossRef]

27. Tian, B.; Zhang, J.; Tong, T.; Chen, F. Preparation of Au/TiO$_2$ catalysts from Au(I)–thiosulfate complex and study of their photocatalytic activity for the degradation of methyl orange. *Appl. Catal. B Environ.* **2008**, *79*, 394–401. [CrossRef]

Publisher's Note: MDPI stays neutral with regard to jurisdictional claims in published maps and institutional affiliations.